


Nonequilibrium Bose-Einstein condensationVishwanath Shukla ^{*}*Department of Physics, Indian Institute of Technology Kharagpur, Kharagpur 721 302, India*

Sergey Nazarenko

Université Côte d'Azur, CNRS, Institut de Physique de Nice, Parc Valrose, 06108 Nice, France

(Received 15 May 2021; revised 10 November 2021; accepted 15 February 2022; published 9 March 2022)

We investigate formation of Bose-Einstein condensates under nonequilibrium conditions using numerical simulations of the three-dimensional Gross-Pitaevskii equation. For this, we set initial random weakly nonlinear excitations and the forcing at high wave numbers and study propagation of the turbulent spectrum toward the low wave numbers. Our primary goal is to compare the results for the evolving spectrum with the previous results obtained for the kinetic equation of weak wave turbulence. We demonstrate existence of a regime for which good agreement with the wave turbulence results is found in terms of the main features of the previously discussed self-similar solution. In particular, we find a reasonable agreement with the low-frequency and the high-frequency power-law asymptotics of the evolving solution, including the anomalous power-law exponent $x^* \approx 1.24$ for the three-dimensional wave action spectrum. We also study the regimes of very weak turbulence when the evolution is affected by the discreteness of the Fourier space, and the strong turbulence regime when the emerging condensate modifies the wave dynamics and leads to formation of strongly nonlinear filamentary vortices.

DOI: [10.1103/PhysRevA.105.033305](https://doi.org/10.1103/PhysRevA.105.033305)**I. INTRODUCTION**

Bose-Einstein condensation (BEC), a macroscopic quantum phenomenon, is now routinely realized in laboratory experiments in systems involving ultracold atoms, polaritons-excitons, photons, magnons, etc. Moreover, BECs are suggested to play an important role in the physics of astrophysical objects, such as neutron stars [1–6] and provide interesting analogies in cosmology [7–9]. Formation of BEC under equilibrium settings and its properties have been extensively studied since the prediction of the phenomenon. Its connection with the phenomenon of superfluidity and the later experimental realizations in different systems makes it one of the most fascinating but challenging quantum many-body systems with many nontrivial macroscopic effects [10,11].

Paths leading to a BEC need not be in equilibrium, it is well known that ultracold Bose gases under cooling quenches pass through highly nonequilibrium states and may eventually lead to the formation of a condensate [12–19]. This nonequilibrium relaxation dynamics of the quantum Bose gases and other quantum many-body systems has attracted a major attention, still the full understanding and characterization of the ensuing dynamics is far from complete [20–28]. It has been argued that the dynamical evolution depends on the strength and nature of the cooling quench in closed systems leading to either wave turbulence-dominated states [29–33] or nonthermal fixed points with universal scaling laws [16,17,34,35].

Important insights into the dynamical evolution of such systems have been obtained based on the Boltzmann-like kinetic description involving the particle momentum distribution function [36–42]. It has been suggested that the system passes through three stages: In the first stage the distribution function undergoes a kinetic redistribution, essentially transporting particles in momentum space towards lower momenta; the second stage is characterized by the nucleation of a condensate; finally, the third stage involves growth of the condensate and its interaction with uncondensed particles. However, the kinetic approach is not applicable for the second stage, so it cannot describe the development of coherence [39,40,42].

A more general framework to study the nonlinear nonequilibrium dynamical evolution of either quenched or forced-dissipated systems of weakly interacting ultracold Bose gases is the Gross-Pitaevskii equation (GPE) and its variants that provide a semiclassical description [31,43–45]. GPE is also referred to as the nonlinear Schrödinger equation. GPE-based theories can describe the dynamics of the uncondensed waves, formation of the condensate and, subsequently, its interaction with the uncondensed component both in equilibrium and out of it [32,46–49]. Moreover, it provides a quantitative description of weakly interacting BECs, whereas it applies only qualitatively if the boson-boson interactions are strong, for example, in the case of superfluid helium. Therefore, it seems to be an appropriate choice to examine the postquench dynamics of both closed and open systems. In particular, our emphasis in this paper is on the forced-dissipated systems to understand the universal features of the dynamics leading to the condensation and test them against the theoretical wave

^{*}research.vishwanath@gmail.com

turbulence predictions and existing numerical simulations of the wave-kinetic equation (WKE). This may also serve as a broad qualitative and an oversimplified model for exciton-polariton condensates or certain astrophysical systems, such as Bose stars.

As mentioned above, BEC may occur out of initial states that are far from thermal equilibrium. This situation is particularly interesting because the condensation process in such cases is strongly nonequilibrium, and it shares fundamental features that are common for turbulent systems—cascadelike transfer of excitations through the momentum space. Moreover, in the absence of forcing and dissipation, the system has two conserved quantities the total energy and the total number of particles. Therefore, it has a dual-cascade property similar to the one in turbulence of classical two-dimensional (2D) flows that conserve the total energy and the total enstrophy [29,50–52]. This analogy allows us to interpret the nonequilibrium condensation process as an inverse cascade of mass in the momentum space (i.e., from large to low momenta), whereas the creation of high-momentum particles and their eventual escape from the system (“evaporation”) as a direct energy cascade [51,53]. Of special interest is the universal scaling behavior in the evolving turbulent spectrum that is anticipated and was previously discussed in literature in the context of the nonequilibrium condensation [40,41,54,55].

Our primary objective in this paper is to elucidate the dynamics leading to the formation of a BEC under nonequilibrium settings within the GPE framework in three dimensions (3D). In particular, we numerically solve the GPE in the inverse cascade setting, whereas suppressing the direct energy cascade which occurs alongside it in the dual-cascade scenario discussed above. We compare results so obtained with those of the WKE, including the pre- t_* self-similar behavior and the post- t_* thermalization process, where t_* denotes the finite time in which the WKE-described distribution function blows up to infinity. We also consider setups where the applicability conditions for the WKE are violated (initially or as a result of evolution) either because the nonlinearity is too weak, leading to the k -space discreteness effects, or too strong, leading to presence of coherent structures, such as strong condensate and hydrodynamic vortices.

The remainder of this paper is organized as follows. In Sec. II we give an overview of the GPE framework as appropriate for this paper. Section III provides a brief account of the wave turbulence theory where focus is on the WKE predictions for the nonequilibrium BEC. In Sec. IV we summarize the numerical methods and the parameters that are used in this paper. Section V contains results of our numerical simulations and their discussion, whereas in Sec. VI we give the conclusions drawn from results and discuss the significance of our paper.

II. GROSS-PITAEVSKII THEORY

In the present paper, we study the nonequilibrium condensation by computing the spatio-temporal (ST) evolution of the complex, classical wave-function $\psi(\mathbf{r}, t)$ of a weakly interacting Bose gas described by the GPE, which has been

modified to include forcing and dissipation,

$$i\frac{\partial\psi}{\partial t} = -\alpha\nabla^2\psi + g|\psi|^2\psi + iF(\mathbf{r}, t) - i\nu_h(-\nabla^2)^s\psi, \quad (1)$$

where $\alpha \equiv \hbar/2m$, m is the mass of a constituent boson, \hbar is the Planck constant, and g is the coefficient of nonlinearity, and it controls the effective interaction strength (see Appendix A). To investigate the nonequilibrium Bose-Einstein condensation, we introduce a forcing that excites the system at short length scales. The explicit form of the forcing term F , written in Fourier space, reads $\widehat{F} = f_0 \exp[i\Theta(\mathbf{k}, t)]$ wherein f_0 is the forcing amplitude, which is finite within a wave-number shell $k_{f1} \leq |\mathbf{k}| \leq k_{f2}$ and zero otherwise, and $\Theta(\mathbf{k}, t)$ represents the random (forcing) phase which is uniformly distributed in $(0, 2\pi]$ and independent at each time step and at each wave number. Our attention will be on the range of wave numbers among $k = 0$, the mode at (and near) which the condensation occurs, and the forcing wave numbers. Moreover, in this paper we do not focus on the forward cascade process from the forcing wave numbers to higher wave numbers as the cost of resolving both the cascades in a numerical simulation is prohibitively expensive.

In order to achieve a large range of wave numbers for the inverse cascade, the forcing range boundaries k_{f1} and k_{f2} are shifted to higher wave numbers followed by introduction of a dissipation that acts at still higher wave numbers, effectively killing the forward cascade process. This dissipation mechanism is modeled by using a hyperviscosity represented by the last term in Eq. (1) (with hyperviscosity coefficient $\nu_h = \text{const}$), which is often used in numerical simulations of turbulent flows; see, e.g., Ref. [44]. If used carefully, hyperviscosity helps in obtaining a large wave-number range for a cascade process, whereas avoiding the effects of truncation (finite wave numbers). We do not introduce any dissipation mechanism at large scales (low wave numbers) where condensate is formed. This allows us to obtain nonstationary turbulent states with condensation and study the self-similar evolution that is not influenced by the dissipation.

Note that our forced-dissipated system is not only useful for the theoretical and numerical studies, but it also qualitatively models a recent forced-dissipated BEC experiment where the forcing was performed via “shaking” the retaining trap and the dissipation—via using a finite-height trap allowing energetic atoms to escape from the system [56].

In the absence of forcing and dissipation, the total mass and the total energy of the bosons are conserved

$$M \equiv \int_{\mathcal{V}} d\mathbf{r} \rho(\mathbf{r}, t) = \text{const}, \quad (2)$$

where $\rho(\mathbf{r}, t) \equiv |\psi(\mathbf{r}, t)|^2$ is the condensate mass density, and

$$E \equiv \frac{1}{2} \int_{\mathcal{V}} d\mathbf{r} [\alpha|\nabla\psi(\mathbf{r}, t)|^2 + \frac{g}{2}|\psi(\mathbf{r}, t)|^4] = \text{const}. \quad (3)$$

Here, the integration is performed over the entire volume of the system assuming suitable boundary conditions. In the present paper, \mathcal{V} is a periodic cube of side L in the 3D space. The energy functional serves as a Hamiltonian for the GPE (in the absence of forcing and dissipation) with its quadratic part,

$$E_2 = \frac{\alpha}{2} \int d\mathbf{r} |\nabla\psi(\mathbf{r}, t)|^2, \quad (4)$$

and the quadric part,

$$E_4 = \frac{g}{4} \int d\mathbf{r} \rho(\mathbf{r}, t)^2 \quad (5)$$

corresponding to the linear and the nonlinear terms, respectively.

In the presence of forcing and dissipation, the total mass and energy vary with time. Other useful quantities are the local speed of sound $c = \sqrt{2\alpha g\rho}$, and the healing length $\xi = \sqrt{\alpha/g\rho}$. The healing length quantifies the distance over which the condensate density recovers from being zero at infinitely hard confining walls to a bulk value; it also gives the radius of the superfluid vortex core. Note that $4\pi\alpha = \hbar/m$ is the quantum of circulation.

III. WAVE TURBULENCE PREDICTIONS

A strongly turbulent state of a 3D superfluid involves an interacting dynamic tangle of quantized vortices on top of a condensate in the presence of random waves and other coherent structures. But strong turbulence is not the only possibility: Nonlinearly interacting random waves give rise to an out-of-equilibrium system, called wave turbulence, characterized by the presence of inter-length-scale transfers (cascades) of certain (conserved) quantities. An important role in understanding turbulent BEC and the processes leading to its formation, is played by the statistical description of random weakly nonlinear waves—the so-called wave turbulence theory (WTT) [29,40–42,51,54,57].

The WTT starts by considering the wave system in a periodic box of side L , in the present case a cubic domain of volume $\mathcal{V} = L^3$. The waves constituting the system are *assumed* to have random independent phases and amplitudes (RPA) at each wave number. Moreover, in WTT the infinite box limit $L \rightarrow \infty$ is taken before the weak-nonlinearity limit, which means that there is a large number of quasiresonances each of which is as important as the exact wave resonance (for a detailed discussion see Ref. [51]). One of the important objects in WTT is the wave action spectrum. For our system, it is defined as

$$n(\mathbf{k}, t) = \lim_{L \rightarrow \infty} \left[\frac{L^3}{(2\pi)^3} \langle |\hat{\psi}(\mathbf{k}, t)|^2 \rangle \right], \quad (6)$$

where $\hat{\psi}$ is the Fourier coefficient,

$$\hat{\psi}(\mathbf{k}, t) = \frac{1}{L^3} \int_{\mathcal{V}} d\mathbf{r} \psi(\mathbf{r}, t) e^{-i(\mathbf{k}\cdot\mathbf{x})}, \quad (7)$$

and $\langle \cdot \rangle$ denotes the RPA averaging.

The WTT analysis of the GPE (1), in the absence of forcing and dissipation, along with the assumption of isotropy leads to the following WKE for the wave action spectrum,

$$\begin{aligned} \frac{\partial n_\omega}{\partial t} &= \pi \omega^{-1/2} \int S(\omega, \omega_1, \omega_2, \omega_3) \delta(\omega + \omega_1 - \omega_2 - \omega_3) \\ &\times n_\omega n_1 n_2 n_3 (n_\omega^{-1} + n_1^{-1} - n_2^{-1} - n_3^{-1}) d\omega_1 d\omega_2 d\omega_3, \end{aligned} \quad (8)$$

see, e.g., Ref. [29]. Observe that we have switched from the wave number to the frequency space: $n_\omega(t) = n[k(\omega), t]$,

where $\omega(k) = k^2$ is the wave frequency $k = |\mathbf{k}|$ and have introduced shorthand notations $n_i = n(\omega_i, t)$, $\omega_i = k_i^2$, $i = 1-3$. The integral in (8) is taken over the positive values of ω_1 , ω_2 , and ω_3 . The kernel of the integral is

$$S(\omega, \omega_1, \omega_2, \omega_3) = \min(\sqrt{\omega}, \sqrt{\omega_1}, \sqrt{\omega_2}, \sqrt{\omega_3}). \quad (9)$$

Like the original GPE (1), Eq. (8) conserves the total mass and the total energy, which now look as follows:

$$M = 2\pi \int_0^\infty \omega^{1/2} n_\omega d\omega, \quad (10)$$

and

$$E = 2\pi \int_0^\infty \omega^{3/2} n_\omega d\omega. \quad (11)$$

Equation (8) has two thermodynamic equilibrium solutions $n_\omega = \text{const}$ and $n_\omega \sim \omega^{-1}$ corresponding to the particle and the energy equipartition in the 3D k space, respectively. It also has two nonequilibrium stationary power-law spectra $n_\omega \sim \omega^{-x}$ with $x = 7/6$ and $x = 3/2$. These are the Kolmogorov-Zakharov (KZ) spectra corresponding to the inverse and direct cascades of M and E , respectively [29,51].

The nonstationary solutions of the WKE (8) in the condensation (inverse cascade) settings were studied numerically in Refs. [40–42,54]. The spectrum was shown to have a tendency to blow up to infinity in a finite time t_* at $\omega = 0$ (corresponding to $k = 0$). Moreover, these studies showed that a power-law behavior $n_\omega(t) \sim \omega^{-x_*}$ starts to develop in the tail and invades the whole inverse cascade range as $t \rightarrow t_*$. Naively, one could think that this power law has exponent $7/6$ as in the inverse cascade KZ spectrum. This statement was indeed made in Refs. [38,39] but later proven wrong in Refs. [40–42,54] wherein the numerically observed exponent is in the range of $x_* \approx 1.23$ to 1.24 , which is clearly different from the exponent $7/6 \approx 1.167$.

The blowup behavior of the solution was attributed to its property of self-similarity of the second kind. According to the Zeldovich-Raizer classification scheme, a solution whose similarity properties cannot be fully determined from a conservation law (conservation of mass in our case) has the self-similarity of the second kind [58]. This is because the self-similar part of the evolving solution contains only a tiny part of the total mass. (The respective spectrum is said to have a finite capacity.) As a consequence, one cannot find the exponent x_* of the asymptotic tail exactly: One has to solve a “nonlinear eigenvalue problem.” Such a nonlinear eigenvalue problem was addressed directly in Ref. [55] where the self-similar solution to the WKE was found with $\sim 5\%$ accuracy and with $x_* \approx 1.22$. In this paper, the low-frequency asymptotics of the spectrum was rigorously proven to be independent of the frequency—a property which was previously observed numerically in Refs. [40,41]. As we see, both direct solutions of WKE (8) to find the evolving spectrum and the solution of (8) restricted to the similarity ansatz lead to mutually consistent results.

Furthermore, it was argued in Refs. [40,41] and supported by numerical simulations of the Boltzmann kinetic equations that the postblowup evolution leads to the creation of a condensate and a thermalized component whose spectral signatures are the formation of a Dirac- δ spectrum at $k = 0$

and an equipartition of energy for the $k \neq 0$ wave numbers, respectively.

Before concluding this section, below we briefly mention three facts from the WTT that will be required for the discussion of our results, for a detailed account of these, see Ref. [51].

(A) The leading-order nonlinear effect in the four-wave systems is actually not the spectrum evolution described by the WKE but a nonlinear frequency shift Ω that leaves the spectrum unchanged

$$\Omega = 2g\langle\rho\rangle. \quad (12)$$

This frequency shift will be seen in the spatiotemporal spectra measured in our simulations.

(B) Apart from the small nonlinearity, the applicability of the WKE requires that the finite-box effect and associated with it the discreteness of the k space are not important. This means that the nonlinear frequency broadening δ_ω (which is on the order of inverse characteristic time of the spectrum evolution τ_{WKE}) must be larger than the distance between adjacent linear-wave frequencies $\Delta\omega \approx (d\omega_k/dk)\Delta k = 2\alpha k(2\pi/L)$.

(C) All of the WTT theory described above, including WKE (8), refers to the four-wave regime characterized by a small nonlinearity,

$$\eta = \frac{E_4}{E_2} \ll 1. \quad (13)$$

However, if during the course of the evolution the condensate present at $k = 0$ grows to a large value, then it starts to affect the dynamics of the uncondensed waves with $k \neq 0$. Moreover, if the condensate fraction $M_0/M \sim 1$, then such waves can be regarded as small perturbations $\tilde{\psi}$ over a strong uniform condensate state ψ_0 (in the physical space), i.e., $|\tilde{\psi}| \ll |\psi_0|$. Under these circumstances, such waves acquire acoustic properties and their frequency satisfies the so-called Bogoliubov dispersion relation [59],

$$\omega_B(k) = g|\psi_0|^2 \pm \sqrt{2g|\psi_0|^2k^2 + \alpha k^4}. \quad (14)$$

It is well known that this regime can also be described within the framework of the WTT and results in a three-wave WKE [29,51]. In this paper, we will observe such an acoustic regime when the condensate fraction reaches a high value close to one. We will examine the realizability of the Bogoliubov dispersion relation Eq. (14), but we will not discuss the spectral evolution governed by the three-wave WKE.

IV. NUMERICAL SETUP

We perform direct numerical simulations (DNS) of the forced-dissipated GPE by using a pseudospectral method over triply periodic cubic domain \mathcal{V} with volume $(2\pi)^3$ using $N_c^3 = 512^3$ collocation points. In this method, we evaluate the linear terms in Fourier space and the nonlinear term in the physical space, which we then transform to Fourier space. To this end, we use the GPE solver of our general purpose code “VIKSHOBHA” [60] wherein we use the FFTW library to compute Fourier-transform operations [61]. A fourth-order Runge-Kutta scheme is used to evolve these equations in time [62]. Limited computational resources did not allow us to perform ensemble averaging over different realizations of

TABLE I. The parameter α fixes the quantum of circulation $4\pi\alpha = h/m$ for a particular run. Parameters α , $c^* = 1$, and $\rho^* = 1$ fix the length scale ξ^* (ξ for the initial state). f_0 is the forcing amplitude.

Run	α	ξ^*	$g = c^{*2}/2\alpha\rho^*$	f_0
Run 1	0.0347	0.0491	14.41	10^8
Run 2	0.0347	0.0491	14.41	10^7
Run 3	0.0087	0.0123	57.47	10^8

forcing, which, in fact, is computationally extremely demanding given the duration of runs that we consider.

Fixing the values of ρ , c , and α in the absence of forcing and dissipation, fixes the variables ξ and g . However, in the presence of forcing and dissipation, the volume-averaged density $\langle\rho(t)\rangle$ varies with time which, in turn, makes c and ξ time dependent. Therefore, in our simulations presented here, we choose an initial state such that $\langle\rho\rangle = \rho^* = 1$, $c = c^* = 1$ [63]. Furthermore, in all our runs we choose the hyperviscosity coefficient $\nu_h = 10^{-35}$ (see Appendix C) and use the boundaries of the forcing range at $k_{f1} = 130$ and $k_{f2} = 131$. Forcing amplitude f_0 and the parameter α used in different simulations are shown in Table I. Moreover, we use these to construct units of length $\xi^* = \sqrt{2\alpha}/c^*$, time $t^* = \xi^*/c^*$ (not to be confused with the blowup time t_*), and energy density $E^* = \rho^*c^{*2}$. Note that ξ^* is the initial healing length, which is used as a reference length scale for the run (the true healing length evolves in time).

V. RESULTS

First of all, we note that larger forcing amplitude f_0 and smaller coefficient α (hence, larger g) mean stronger initial degree of nonlinearity of the system. Thus, among the runs listed in Table I, Run 3 has the highest and Run 2 has the lowest nonlinearity. This agrees with Fig. 1(a) where the evolution of the ratio of the quadric to quadratic parts of the energy η is shown for the three runs. (Recall that the quadratic and the quadric energies correspond to the linear and the nonlinear dynamics, respectively.) The initial rapid decrease in η is an artifact of the choice of initial condition $\langle\rho\rangle = 1$ at $t = 0$; this continues until forcing starts to dominate the dynamics. Nonetheless, after an initial adjustment and up until $t/t^* \approx 2000$ even Run 3 remains relatively weakly nonlinear with $\eta < 0.2$. Nonlinearities of the runs Run 1 and Run 2 remain rather weak through their entire durations (very weak for Run 2). Note that the normalized durations of the runs Run 1 and Run 2 were much less than the one of Run 3 because their respective values of the characteristic time t^* are much longer.

Figure 1(b) shows the evolution of the condensate fraction M_0/M in the $k = 0$ mode for the runs Run 1–Run 3. We find that in Run 2 the condensate fraction unexpectedly grows to a large value of ($M_0/M \sim 0.65$), even though it has the lowest value of nonlinearity among the three runs. This observation is counterintuitive; we discuss its plausible explanation later in this section. It must also be mentioned that even though the condensate fraction is high, its absolute value remains rather small ($\rho_0 \sim 0.1$ with total density $\rho \sim 0.2$). Moreover,

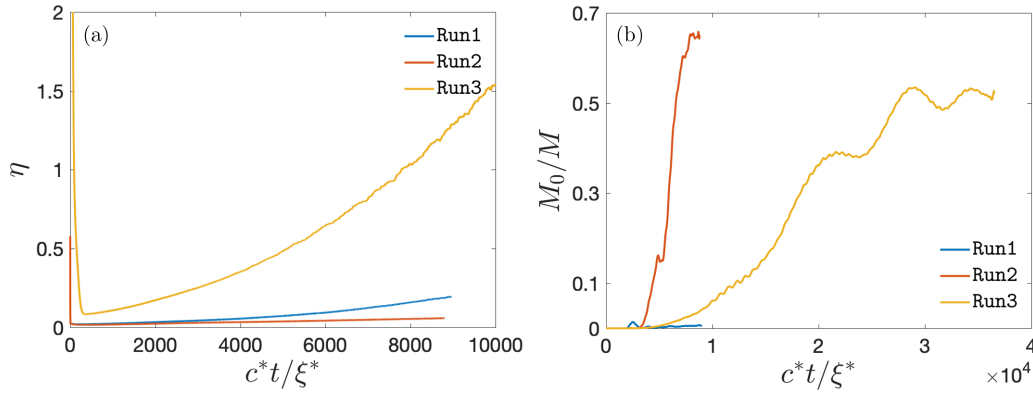


FIG. 1. Temporal evolution of (a) nonlinearity parameter $\eta = E_4/E_2$ [see Eqs. (4), (5), and (13) for the definitions], (b) the condensate fraction M_0/M .

we will see that it does not affect the dispersion properties of the uncondensed excitations ($k \neq 0$). Run 3 exhibits the second strongest condensate fraction ($M_0/M \sim 0.5$), and despite being strongly nonlinear, the condensate growth is smaller than what is observed in Run 2 (when the growth interval is measured in units of t^*). However, the condensate fraction in case of Run 1 (with intermediate nonlinearity) remained vanishingly small throughout the duration of the run.

In Figs. 2 and 3 we show one-dimensional (1D) wave-action spectra at different moments of time computed for the runs Run 1–Run 3. We obtain a 1D wave-action spectrum $n^{1D}(k, t)$ by summing the 3D spectra $\sim |\hat{\psi}(\mathbf{k}, t)|^2$ in a spherical shell of radius k and thickness δk and dividing by δk . In other words, $n^{1D}(k, t)$ is the wave-action density in $k = |\mathbf{k}|$; the angle dependence is erased as the system is expected to be approximately statistically isotropic. Moreover, for future reference, we find it pertinent to mention that the power spectrum $n_\omega \sim \omega^{-x}$ written in terms of frequency ω corresponds to the wave-action spectrum $n^{1D}(k) \sim k^{2-2x}$.

From the plots in Figs. 2 and 3, we observe that the spectra are in qualitative (and to a varying degree in quantitative) agreement with the WTT results obtained by numerically solving the WKE (8). Namely, the plots in Figs. 2 and 3 are consistent with the preblowup and the postblowup behaviors. Indeed, the early evolution in Fig. 2 exhibits emergence of

a power-law scaling $n^{1D}(k) \sim k^2$ which corresponds to $n_\omega \sim \text{const}$; this is in agreement with the low-frequency asymptotics of the self-similar solution of the WKE. This is followed by the development of a second power-law scaling region at the higher- k side of the inverse cascade range with slopes ~ -0.58 in Run 1, ~ -0.80 in Run 2, and ~ -0.52 in Run 3 that correspond to exponents $x \approx 1.29, 1.40$, and 1.26 , respectively, for n_ω . Note that these slopes are computed over the range $1/\xi < k < k_{f1}$ because for $k \lesssim 1/\xi$ the nonlinearity fails to be weak (see Appendix C). It is evident that these exponents are close to the values obtained for the self-similar solution of the WKE, $x_* \approx 1.22$ – 1.24 , for details see Sec. III. Later, we will discuss the possible reason why Run 3 gives the closest result.

The late-time behavior shown in Fig. 3 is consistent with the post- t_* behavior of the WKE evolution. For all three runs, at the higher- k end of the inverse cascade range, we observe formation of a plateau $n^{1D}(k) \sim \text{const}$ which corresponds to the thermodynamic energy equipartition $n_\omega \sim 1/\omega$. At the lowest wave numbers we observe a sharply peaked spectrum that appears to decay as $k^{-2.5}$ instead of the predicted infinitely thin (Dirac- δ) distribution at $k = 0$ mode representing the condensate. It is natural that such an idealized distribution is not observed in our DNS because the low- k dynamics is affected by both the finite size of the system and an enhanced

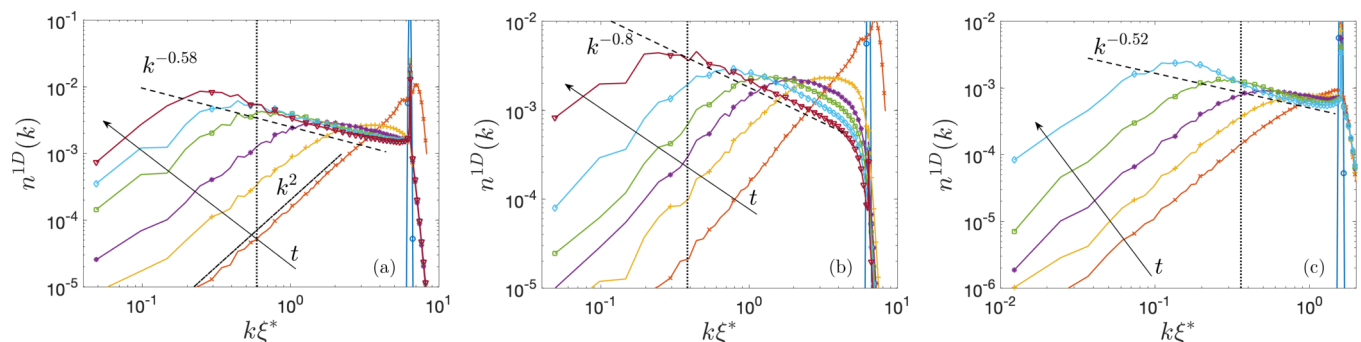


FIG. 2. Temporal evolution of spectra $n^{1D}(k)$ vs k at early stages of our numerical simulations. Plots (a)–(c) correspond to Run 1 ($0 \leq t c^*/\xi^* \leq 1.93 \times 10^3$), Run 2 ($0 \leq t c^*/\xi^* \leq 2.54 \times 10^3$), and Run 3 ($0 \leq t c^*/\xi^* \leq 2.0 \times 10^3$), respectively. The vertical dotted line indicates the position of $k\xi(t) \sim 1$ at the latest moment of time. The various slopes shown here by dashed lines represent power-law fits in the interval $(1/\xi, k_{f1})$ at the latest time. The dot-dashed line in (a) shows the k^2 scaling at small wave numbers.

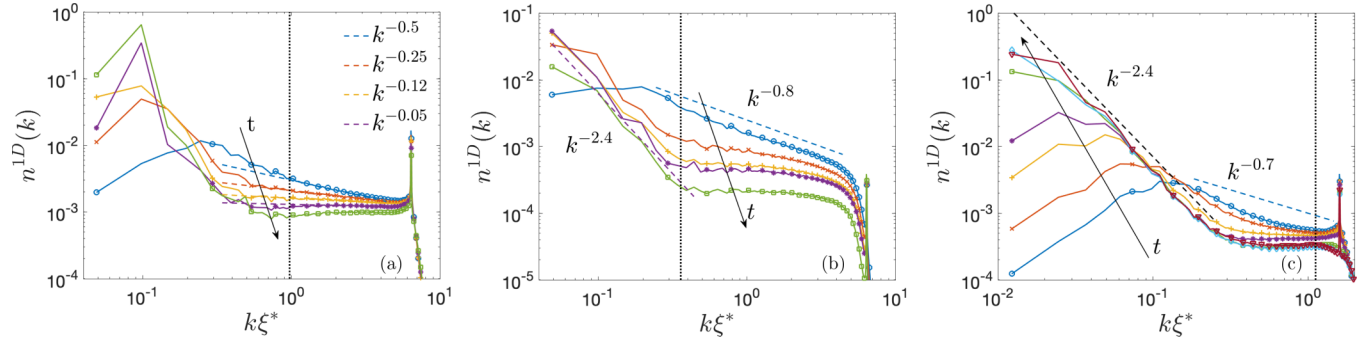


FIG. 3. Temporal evolution of spectra $n^{1D}(k)$ at later stages of our numerical simulations. Plots (a)–(c) correspond to Run 1 ($2.03 \times 10^3 \leq t c^*/\xi^* \leq 8.95 \times 10^3$), Run 2 ($3.05 \times 10^3 \leq t c^*/\xi^* \leq 8.80 \times 10^3$), and Run 3 ($2.08 \times 10^3 \leq t c^*/\xi^* \leq 3.64 \times 10^4$), respectively. The vertical dotted line indicates the position of $k\xi(t) \sim 1$. The various slopes shown here by dashed lines indicate power-law fits to the spectra at different times.

nonlinearity. Thus, the condensate emerging in our simulations is imperfect: It contains space-time-dependent strongly nonlinear coherent structures, and we will revisit this again later. The slope -2.5 for the 1D wave-action spectrum is rather close to the low- k slope -3 (-5 for the 3D wave-action spectrum) observed in a closed system for a freely decaying initial condition (no forcing or dissipation) in Ref. [17] where a scaling argument suggested that the -3 slope should be observed for strong turbulence.

Figure 3(a) for Run 1 shows that $n^{1D}(k)$ spectra at later stages of the simulation exhibits a pronounced peak at small wave numbers around $k\xi^* = 0.1$, which appears to be continually growing. Therefore, the condensate fraction is expected to grow further, if the simulation is run longer.

Also note that both the condensate and the plateau region in the spectrum at late times for Run 3 are located at the wave numbers well below $1/\xi$. This means that the influence of the condensate onto the high- k modes is significant: These modes behave as sound waves and, therefore, are not described by the four-wave WKE (8); see Sec. III. However, it is interesting to observe that the energy equipartition spectrum in this case as well is given by $n^{1D}(k) \sim \text{const}$, which for the present state is called the Bogoliubov spectrum [32,33,44,64].

Next we make use of the ST spectra of field $\psi(\mathbf{r}, t)$ to characterize and emphasize the differences between different stages of the evolution of our three runs Run 1–Run 3. The ST spectrum gives the power spectrum of a given quantity as a

function of wave number and frequency. In Figs. 4–6 we show these ST spectra for the runs Run 1–Run 3. We compute ST spectra by performing Fourier transform over a finite window of size T which is greater than the linear wave period and less than the characteristic time over which the spectrum evolves. Since the spectrum is nearly isotropic, we choose $k_y = 0$ and perform the Fourier transform in time for each (k_x, k_z) ; this is followed by angle averaging on the (k_x, k_z) plane to finally obtain ST spectra as a function of $k = \sqrt{k_x^2 + k_z^2}$ and ω . Moreover, plots in Figs. 4–6 are presented in such a way that at each k we normalize the integral over ω to the same constant; this allows us to see the details of the spectrum at each k clearly, even though its value varies over many orders of magnitude in the k range.

Before proceeding further, we remark that a weak nonlinearity manifests itself in the form of a narrow distribution of the ST spectrum around the linear dispersion relation $\omega_k = \alpha k^2$, along with a small nonlinear correction $\Omega = 2gM/L^3$. This is indeed what we find during the initial evolution as shown in the plots of Figs. 4–6. Late evolution in Run 1 is characterized by very similar plots of ST spectra (omitted here) because the condensate fraction remains negligible throughout its duration. On the other hand, late evolution in runs Run 2 and Run 3 is characterized by a large condensate fraction. Hence, it is not surprising that the ST spectra in these cases follow more closely the Bogoliubov dispersion relation

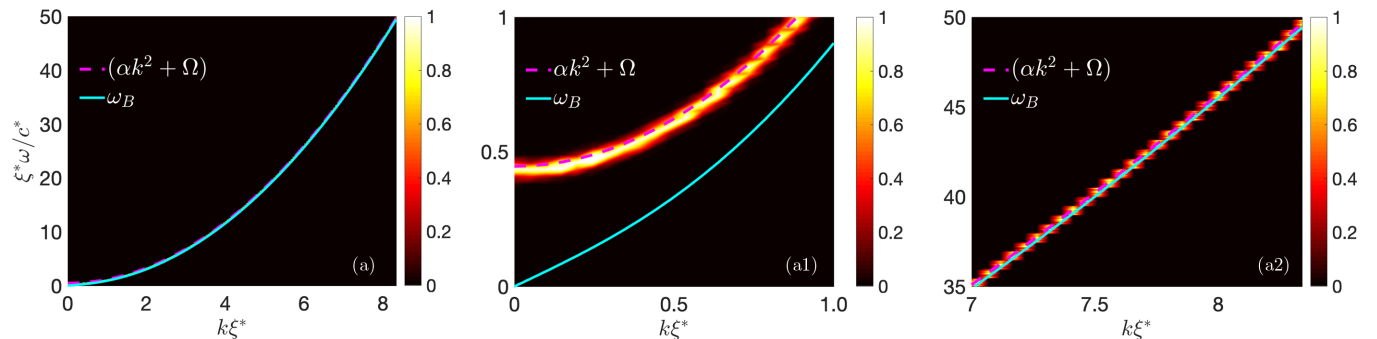


FIG. 4. Plots of spatiotemporal spectra for Run 1 computed over the time interval $1.14 \times 10^3 \leq T c^*/\xi^* \leq 1.37 \times 10^3$. (a) The full spectrum; (a1) and (a2) zoom at small and large wave numbers, respectively. The forcing range is $k_f \xi^* \in (6.3830, 6.4321)$. During the above time interval $n^{1D}(k) \sim k^{-0.58}$, see Fig. 2(a).

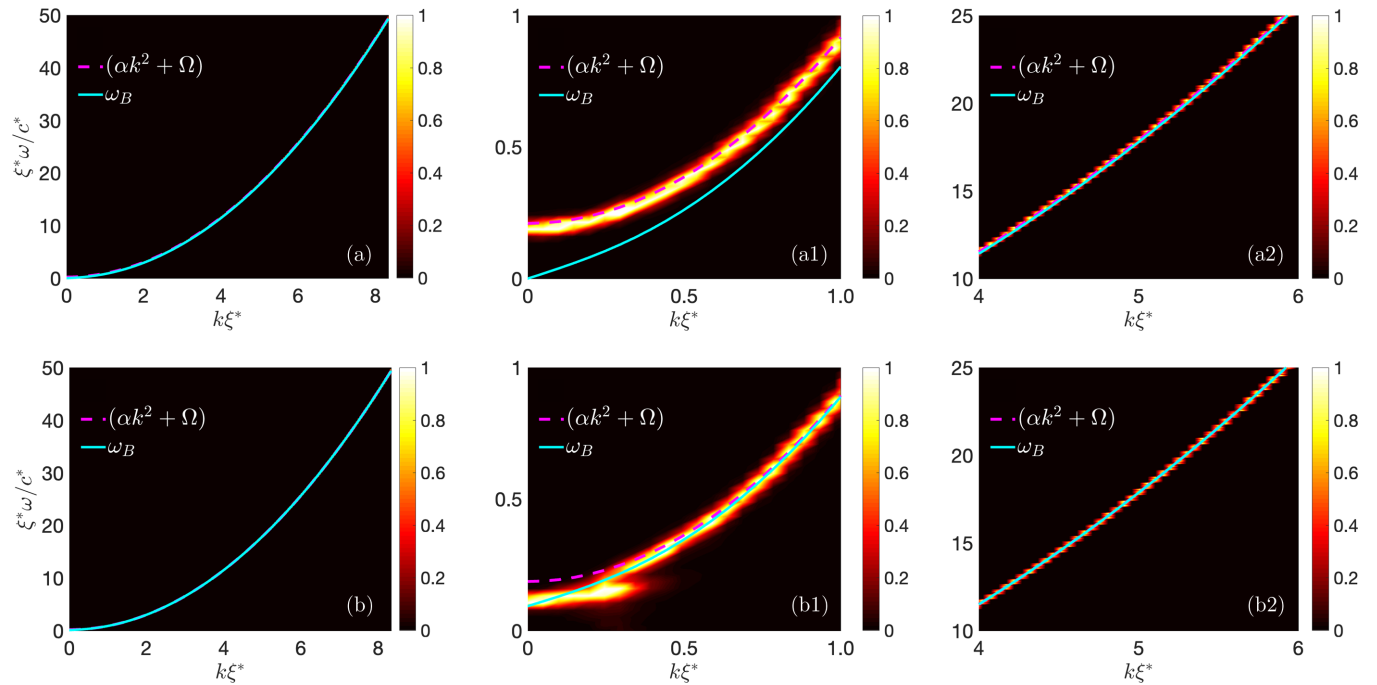


FIG. 5. Plots of spatiotemporal spectra for Run 2. (a) ST spectra computed over the time-interval $2.45 \times 10^3 \leq Tc^*/\xi^* \leq 2.67 \times 10^3$. (a1) and (a2) show a zoom at small and large wave numbers, respectively. During the above time-interval $n^{\text{1D}}(k) \sim k^{-0.8}$, see Fig. 2(b). (b) ST spectra computed over the time interval $6.52 \times 10^3 \leq Tc^*/\xi^* \leq 6.75 \times 10^3$; (b1) and (b2) show a zoom at small and large wave numbers, respectively. The forcing range is $k_f \xi^* \in (6.3830, 6.4321)$.

Eq. (14) rather than $\omega(k) = \alpha k^2 + \Omega$, see the plots (b) and (b1) in Figs. 5–6. Furthermore, in these plots the condensate component shows up as a short piece of horizontal line at

small k 's and $\omega = g\rho$. The fact that the condensate has short but finite range in k means that it is not perfectly uniform in the physical space, whereas the fact that its ST spectrum

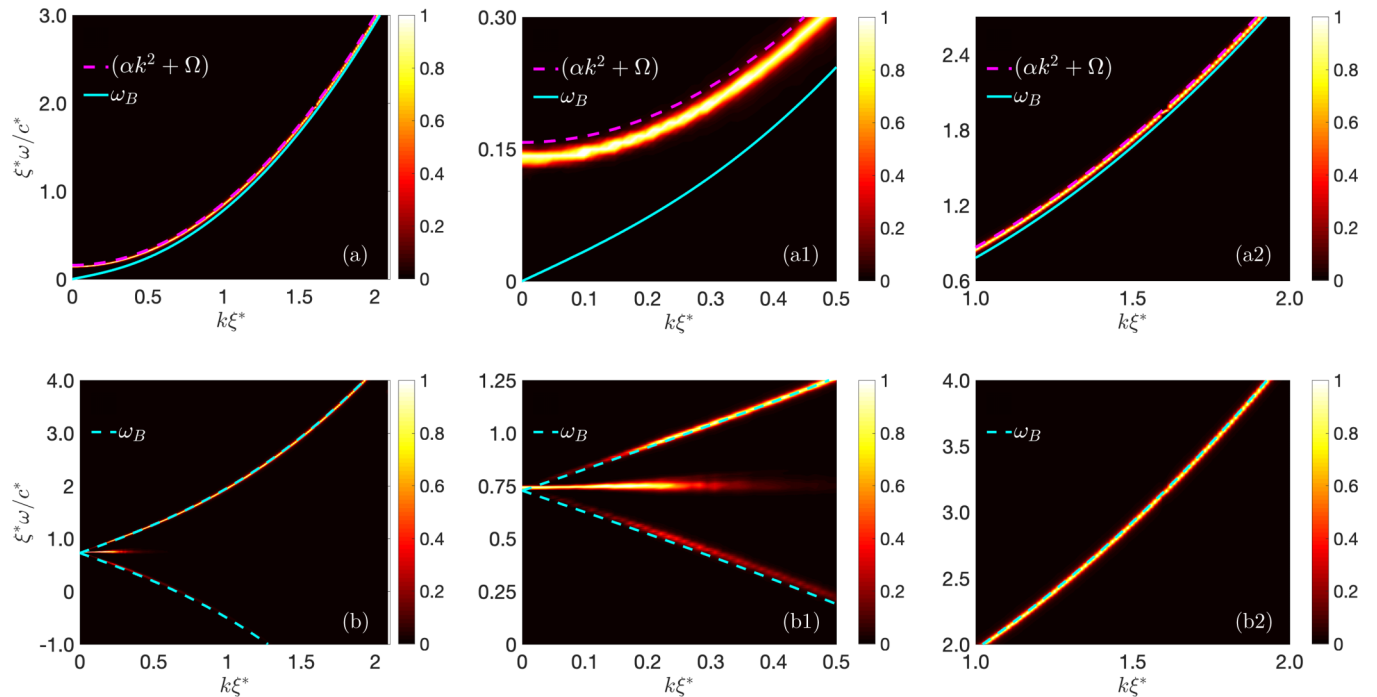


FIG. 6. Plots of spatiotemporal spectra for Run 3. (a) ST spectra computed over the time-interval $1.30 \times 10^3 \leq Tc^*/\xi^* \leq 2.14 \times 10^3$; (a1) and (a2) show a zoom at small and large wave numbers, respectively. During the above time-interval $n^{\text{1D}}(k) \sim k^{-0.52}$, see Fig. 2(c). (b) ST spectra computed over the time-interval $2.80 \times 10^4 \leq Tc^*/\xi^* \leq 2.89 \times 10^4$; (b1) and (b2) show a zoom at small and large wave numbers, respectively. The forcing range is $k_f \xi^* \in (1.5990, 1.6113)$.

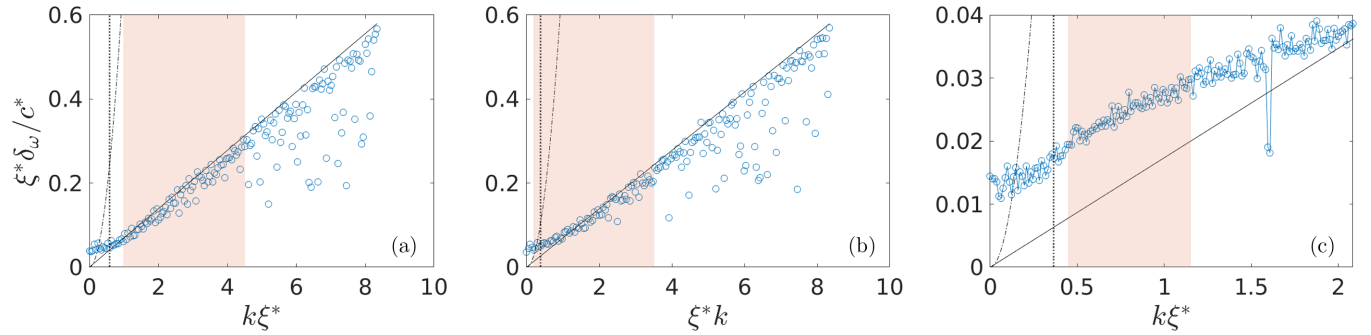


FIG. 7. Spectral broadening δ_ω vs k obtained from the spatiotemporal spectra for Runs: (a) Run 1 ($1.14 \times 10^3 \leq tc^*/\xi^* \leq 1.37 \times 10^3$); (b) Run 2 ($2.45 \times 10^3 \leq tc^*/\xi^* \leq 2.67 \times 10^3$); and (c) Run 3 ($1.30 \times 10^3 \leq tc^*/\xi^* \leq 2.14 \times 10^3$). The vertical dotted line indicates the position of $k\xi(t) \sim 1$ at time: (a) $tc^*/\xi^* = 1.3 \times 10^3$, (b) $tc^*/\xi^* = 2.54 \times 10^3$, and (c) $tc^*/\xi^* = 2.0 \times 10^3$. Shaded area indicates the approximate region over which power-law scaling are observed in Fig. 2. The dashed-dot lines represent the curve αk^2 , whereas solid lines represent $\Delta\omega = 2\alpha k$.

is nearly horizontal means that the condensate represents a coherent component which oscillates at approximately the same frequency as a whole.

Note that the negative frequency branch of the Bogoliubov excitations shows up much more prominently for Run 2 in Figs. 5(b) and 5(b1) than for Run 3 in Figs. 6(b) and 6(b1). This is because Fig. 5 for Run 2 shows that the system is still in the four-wave regime, whereas Fig. 6 for Run 3 the system has moved to a three-wave regime. In the presence of a condensate there are two Bogoliubov branches in the Fourier transform of ψ . Also, the normal modes (a_k and a_{-k}^*) of the Bogoliubov wave are a linear combination of ψ_k and ψ_{-k}^* and vice versa (see Ref. [51] for more details). The lower branch (negative ω) is associated with the contribution of a_k^* . Therefore, the observations of Figs. 6(b) and 6(b1) tell us that the coefficients in front of a_k and a_{-k}^* are unequal and depend on the condensate strength, and here the former gets favored over the latter. Also, Run 3 has the highest nonlinearity and Run 2 the lowest; therefore, in the latter condensate density is extremely small and hardly any (or no) negative frequency branch is present, and the dispersion is primarily $\omega \sim k^2$.

The ST spectra can also be used to measure the nonlinear frequency broadening δ_ω and, therefore, directly examine if the conditions of applicability of the WTT are satisfied. We recall from the previous discussion [see Sec. III point (B)] that for the WTT applicability δ_ω must satisfy $2\alpha k(2\pi/L) = \Delta\omega \ll \delta_\omega \ll \omega_k = \alpha k^2$. On the ST spectra plots, we define δ_ω at each fixed k as the full width at half maximum of the ω peak. Figures 7(a)–7(c) show the plots of δ_ω together with ω_k and $\Delta\omega$ for the three runs. The time intervals for these plots are chosen to be around the time at which the pre- t_* power-law scalings are present, and the shaded regions indicate the k range over which these scalings were observed. We clearly see that the degree of nonlinearity in these scaling intervals is low $\delta_\omega < \omega_k$ as required by the WTT. On the other hand, we see that the condition $\delta_\omega > \Delta\omega$ is well satisfied for Run 3 only. Thus, the applicability of the WTT description is best satisfied in Run 3, which explains why this run gives the best agreement with the WKE result for the pre- t_* power-law exponent x_* (1.26 in Run 3 vs 1.22–1.24 from the WKE simulations). We also recall that the nonlinearity of Run 3 is the highest among the three runs, and it is the higher nonlinearity that

allows it to overcome the effect of discreteness of the k space. Run 1 and Run 2 are both affected by the k -space discreteness [65]. However, the nonlinearity of Run 1 is higher than the one of Run 2, and it is, therefore, natural that the pre- t_* power-law exponent x_* in Run 1 is closer to the WKE result (1.28 and 1.40 in Run 1 and Run 2, respectively, vs 1.22–1.24 from the WKE simulations).

It is interesting to note that the nonlinear frequency broadening has qualitatively the same behavior in the plots (a) and (b) of Fig. 7, even though the degree of nonlinearity of runs Run 1 and Run 2 are very different: It is in approximate balance with the linear wave frequency spacing $\delta_\omega \sim \Delta\omega$, which is particularly clear in the scaling range. A possible explanation for this behavior is a sandpile effect which was initially discussed in the context of water waves [66]. In forced systems, the turbulent cascade (the inverse cascade of mass in our case) is initially impeded by the discreteness of the Fourier space because there are less frequency and wave number resonances in the discrete k space compared to the continuous one. Given that the system is continuously forced, it will result in an accumulation on the spectrum in the vicinity of the forcing wave number, which, in turn, will lead to an increase in the nonlinear broadening δ_ω . This spectrum accumulation will continue until δ_ω reaches the typical values of $\Delta\omega$ at which point the quasinormal modes will become active and will trigger the turbulent cascade in the k space. Then turbulent cascade will start to deplete the accumulated spectrum and if the forcing is weak the broadening δ_ω will return to the critical values with $\delta_\omega(k) \sim \Delta\omega(k)$, but not below it because this would switch off the quasinormal modes and re-initiate the spectrum accumulation. Of course, such a sandpile scenario is very speculative and can be only taken as a plausible explanation of the observed behavior.

We now return to the discussion of the emergence of the condensate as a result of the inverse cascade process. We have already mentioned, whereas discussing the features of the ST spectra, that the condensate is imperfect: It is nonuniform in the physical space. In Figs. 8(a)–8(c) we show the isosurface plots of density $\rho(\mathbf{r}, t)$ for the runs Run 1 at $\rho = 0.055\langle\rho\rangle$, Run 2 at $\rho = 0.023\langle\rho\rangle$, and Run 3 at $\rho = 0.49\langle\rho\rangle$, respectively, at times not far from the end of these runs. The chosen threshold values allow us to visualize quantum

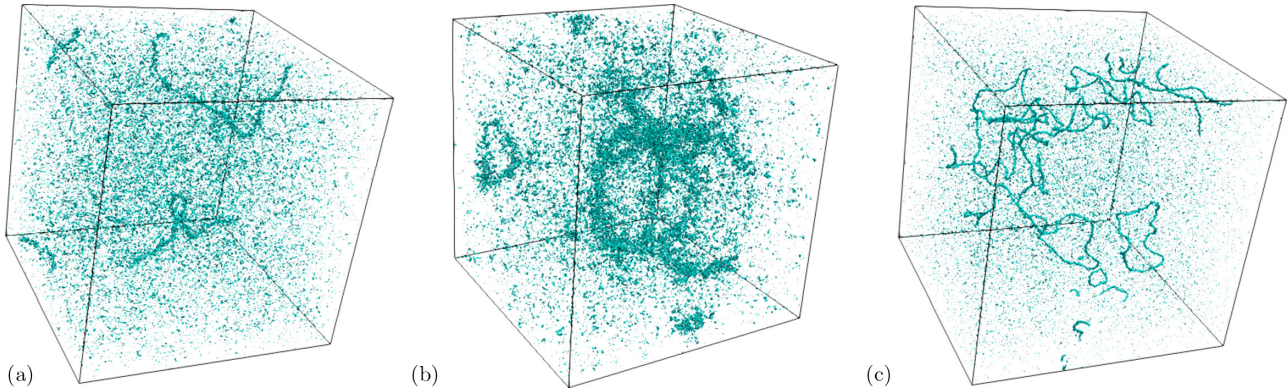


FIG. 8. Isosurface plots of the condensate density for the runs: (a) Run 1 at $tc^*/\xi^* = 8.5 \times 10^3$ for $\langle \rho \rangle / \rho^* = 0.055$; (b) Run 2 at $tc^*/\xi^* = 6.75 \times 10^3$ for $\langle \rho \rangle / \rho^* = 0.023$; (c) Run 3 at $tc^*/\xi^* = 2.89 \times 10^4$ for $\langle \rho \rangle / \rho^* = 0.49$. Visualization is for the entire simulation domain $L^3 = (2\pi)^3$.

vortices clearly. We remind that at the vortex center $\rho = 0$ and at distances $\sim \xi$ away from it the density ρ goes back to the values of the surrounding medium (hence, the name healing length). In Run 2 and Run 3 we see a few well-formed vortex lines, which is not surprising, because the condensate fraction reaches rather high values by the end of these simulations (even though the global nonlinearity parameter η in Run 2 remains very low). These vortices are sometimes called phase defects—they are the physical space manifestations of the condensate imperfection. What is surprising, however, is that the large-scale vortexlike structures are also seen in Run 1 wherein the condensate fraction remains tiny. Note that the presence of large density fluctuations render this vortex-loop fuzzy and result in the appearance of what are called “ghost vortices,” which are not actual vortices but merely regions of zero density, but the overall large-scale coherence of such vortices is evident. Thus, large-scale vortices seem to be robust structures even in cases without well-formed condensate.

Finally, as we had remarked earlier, we are puzzled by the fact that the condensate fraction in Run 2 grows to a large value, whereas it remains tiny in Run 1, even though the latter is more strongly nonlinear than the former. It seems that the discreteness of the k space, which is a significant factor in Run 2, helps in the steady growth of the $k = 0$ component. A possible reason behind this could be that it is harder to “spill out” particles from the $k = 0$ mode into the neighboring modes when the dynamics is strongly restricted by the k -space discreteness. However, further studies are required to better understand this phenomenon.

VI. CONCLUSIONS

We have elucidated the inverse cascade process that leads to the Bose-Einstein condensation under nonequilibrium conditions within the framework of the force-dissipated GPE. Results obtained from the DNS of the GPE equation in the WTT regime are in agreement with the WKE predictions both the pre- t_* self-similar behavior leading to blow up in a finite time and appearance of a condensate and the thermalization process that ensues after time t_* . We find that the characteristics of the inverse cascade regime that develops is strongly dependent on the level of nonlinearity present in the system,

the latter itself varies with time (as we are not investigating steady states).

We were able to identify three regimes with different scaling behaviors during the course of the evolution: (i) at early times the presence of $n^{1D}(k) \sim k^2$ scaling at wave numbers smaller than the forcing wave number; (ii) followed by the emergence of $k^{-\alpha}$ with α between 0.5 and 0.8 for different cases considered here, over wave numbers between $1/\xi$ and the forcing wave number; (iii) finally, $n^{1D}(k)$ tends to develop a plateau with near-zero exponents at wave numbers close but smaller than the forcing wave number, and at still smaller wave numbers we observe a spectrum with a large negative exponent (~ -2.5) associated with development of a condensate at the $k = 0$ mode. Regimes (i) and (ii) correspond to the pre- t_* evolution of the system and at intermediate times these regimes coexist, whereas regime (iii) is associated with the post- t_* dynamics. Our spatiotemporal analysis clearly shows that if the nonlinearity is small and the finite-box effect is negligible, then the four-wave WTT holds, and we obtain $n^{1D}(k) \sim k^{-0.52}$ scaling which is compatible with and corresponds to the WKE predictions of $n_\omega(t) \sim \omega^{-x_*}$ with exponent $x_* \approx 1.23$ to 1.24 . The post- t_* dynamics is dominated, depending on the level of nonlinearity, by weak waves involved in four-wave interactions described by the WTT or by the presence of coherent structures—a strong coherent condensate along with well-developed loops of hydrodynamic vortices. However, in either of these cases the turbulent spectrum is characterized by an energy equipartition at high wave numbers and a steep spectrum at low-wave numbers.

In our simulations, we do not dissipate particles at low-wave numbers. The condensate forming at low wave numbers absorbs particles cascading from the high-wave number region of the spectrum. Naively thinking, eventually we can regard it as an effective particle sink and, therefore, expect the formation of the KZ inverse cascade spectrum with exponent $x = 7/6$. However, our numerical simulations show that this is not the case. Indeed, the condensate component cannot serve as an effective sink of particles: It reflects particles back to the high-wave-number range and a spectrum close to the thermodynamic one forms instead of the KZ spectrum. On the other hand, this leaves unanswered the question if the full or a partial suppression of the condensate component

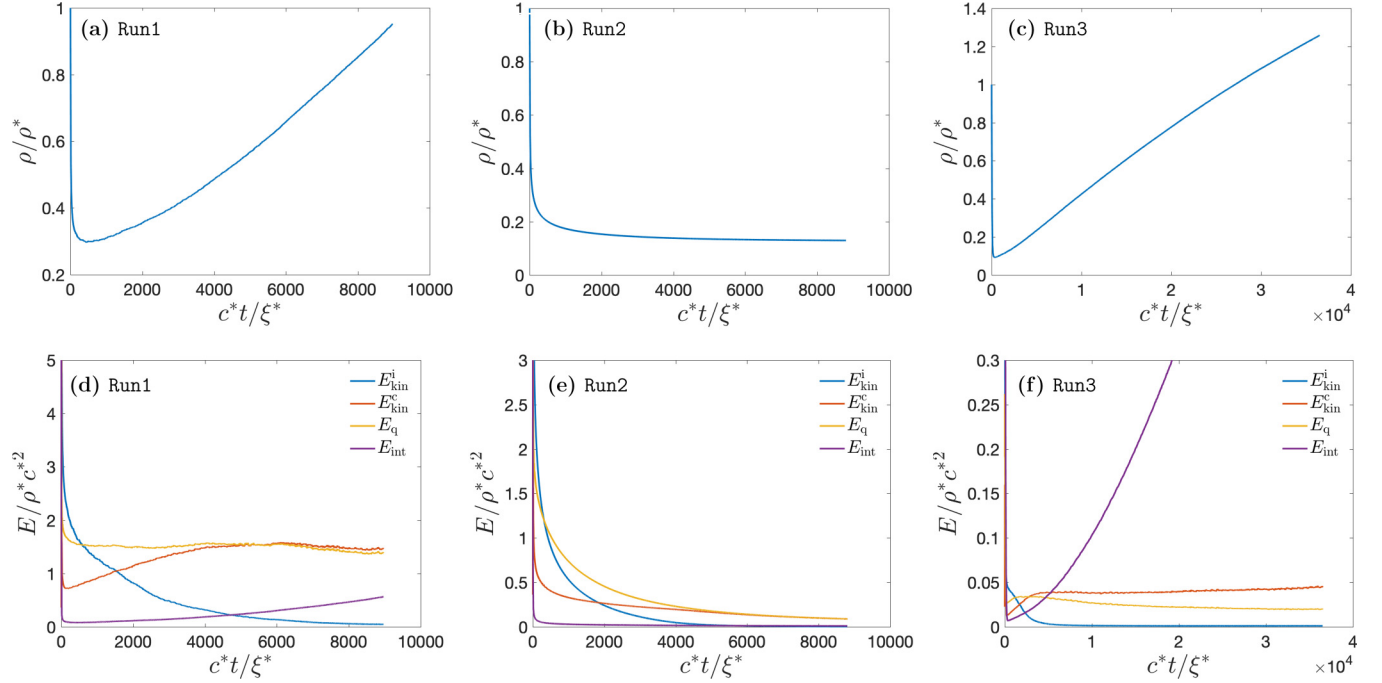


FIG. 9. Temporal evolution of total density [top panel (a)-(c)] and different energy components [bottom panel (d)-(f)] for the runs Run 1, Run 2, and Run 3. E_{kin}^i and E_{kin}^c denote the incompressible and compressible components of the kinetic energy, respectively. E_q and E_{int} denote the quantum pressure energy and the interaction energy, respectively.

(by introducing an extra dissipation mechanism at low-wave numbers) could lead to formation of the stationary KZ spectrum. This question should be studied theoretically and numerically in the future. In the case of the positive answer, one could further investigate if the inverse cascade KZ spectrum could be implemented in a BEC experiment.

ACKNOWLEDGMENTS

Part of this work was granted access to the computing facilities under GENCI (Grand Equipement National de Calcul Intensif) Grant No. A0062A10441 (IDRIS, CINES, and TGCC) and High Performance Computing Facility at IIT Kharagpur established under National Supercomputing Mission (NSM), Government of India and supported by the Centre for Development of Advanced Computing (CDAC), Pune. V.S. acknowledges support from the Start-up Research Grant No. SRG/2020/000993 from SCIENCE & ENGINEERING RESEARCH BOARD (SERB), India. During this project, S.N. was supported by the Chaire D'Excellence IDEX (Initiative of Excellence) awarded by Université de la Côte d'Azur, France, Simons Foundation Collaboration Grant Wave Turbulence (Award No. 651471), the European Unions Horizon 2020 Research and Innovation Programme in the framework of Marie Skłodowska-Curie HALT Project (Grant Agreement No. 823937) and the FET Flagships PhoQuS Project (Grant Agreement No. 820392). V.S. is thankful to K. S. Eswaran for helping with the plots in Fig. 8.

APPENDIX A: FORCED-DISSIPATED GPE

To describe the nonequilibrium states of a system of weakly interacting Bose, in the presence of forcing and

dissipation, we use the following modified Gross-Pitaevskii equation:

$$i\hbar \frac{\partial \Psi}{\partial t} = -\frac{\hbar^2}{2m} \nabla^2 \Psi + g|\Psi|^2 \Psi + \frac{i\hbar}{\sqrt{m}} F(\mathbf{r}, t) - i\hbar v_h (-\nabla^2)^8 \Psi. \quad (\text{A1})$$

Here, in general, the total number of bosons N varies with time and is given by

$$\int_{\mathcal{V}} d\mathbf{r} |\Psi(\mathbf{r}, t)|^2 = N(t). \quad (\text{A2})$$

If we let $\alpha \equiv \hbar/2m$ and define the mass density as

$$\rho(\mathbf{r}, t) \equiv m|\Psi(\mathbf{r}, t)|^2 = |\psi(\mathbf{r}, t)|^2, \quad (\text{A3})$$

then we can write the forced-dissipated GPE as

$$i \frac{\partial \psi}{\partial t} = -\alpha_0 \nabla^2 \psi + g|\psi|^2 \psi + F(\mathbf{r}, t) - i v_h (-\nabla^2)^8 \psi, \quad (\text{A4})$$

where $g \rightarrow g/\hbar m$.

APPENDIX B: TEMPORAL EVOLUTION OF DENSITY AND ENERGY COMPONENTS

In Fig. 9 we show the temporal evolution of the total density (top panel) and different energy components (bottom panel) for runs Run 1, Run 2, and Run 3.

APPENDIX C: A FEW COMMENTS ON THE NUMERICAL SIMULATIONS

1. Hyperviscosity

Turbulence modeling studies, including wave turbulence, frequently use hyperviscosity to avoid wasting numerical

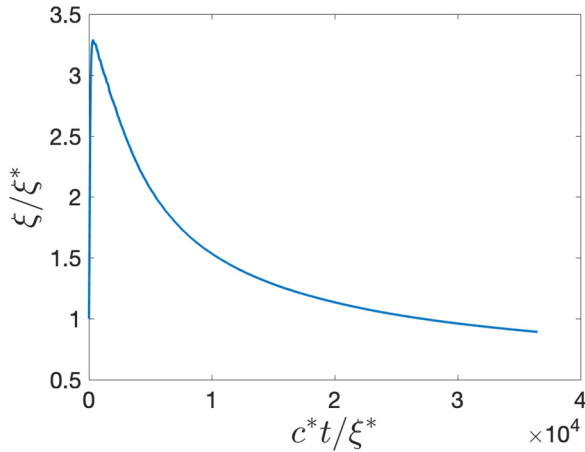


FIG. 10. Temporal evolution of the healing length for Run 3.

resolution by restricting the range of scales over which dissipation occurs (see Refs. [67–69]). This is true for numerical simulations of both 2D and 3D turbulences. For example, in Ref. [69] it was shown that 3D inertial-range dynamics seems to be relatively independent of the form of the hyperviscosity and that modest-resolution simulations with high-order hyperviscosity lead to inertial ranges allowing computation of quantities that are otherwise intractable.

We have used hyperviscosity with a similar aim of providing an effective energy sink at small scales. Such a dissipation is significant only for wave numbers close to $k_d \lesssim$

$k_{\max} = N_c/3$. Therefore, a rough estimate of the coefficient of hyperviscosity can be obtained as follows: $\nu_h k_{\max}^{16} \sim 1$; thus, $\nu_h \sim (3/512)^{16} = 2 \times 10^{-36}$. “Choosing carefully” in our case means avoiding the spectrum pile up near k_{\max} , and the above estimate ensures this; we have used $\nu_h = 10^{-35}$ in all the runs. Varying ν_h (e.g., within an order of magnitude) shows that results are not sensitive to this. Also, note that no fine-tuning of ν_h was performed in order to obtain the desired result.

2. Adequateness of the numerical resolution

Note that the choice of the unit ξ^* is based on the initial condition wherein $\rho = 1$ and $c = 1$. However, during the course of the evolution the density $\rho(t)$ of the system in Run 3 (and all other runs reported here) changes with time as the system is far from a steady state; therefore, the actual healing length $\xi(t) = \sqrt{\alpha/g\rho}$ also varies with time, see Fig. 10 below. The scaling shown in Fig. 2(c) is during a period when the actual healing length $\xi(t)/\xi^* > 2$. Therefore, the healing length is well resolved. Moreover, Fig. 2(c) clearly shows that $1/\xi$ is well separated from k_{\max} . At a later stage $1/\xi$ is closer to k_{\max} [see Fig. 3(c)] and tight discretizations are usual for GPE (turbulence) simulations. Also, the structure of an individual vortex might not be well resolved, but for this late stage we are concerned with scales larger than it. Therefore, even though the vortex cores are not resolved at late times in Run 3, and hence, their motion may alter at higher resolution, but the larger scales should not be affected.

-
- [1] A. B. Migdal, *Nucl. Phys.* **13**, 655 (1959).
- [2] V. L. Ginzburg and D. A. Kirzhnits, *Zh. Eksp. Teor. Fiz.* **46**, 397 (1964) [*J. Exptl. Theoret. Phys. (U.S.S.R.)* **46**, 397 (1964)].
- [3] P. W. Anderson and N. Itoh, *Nature (London)* **256**, 25 (1975).
- [4] P. S. Shternin, D. G. Yakovlev, C. O. Heinke, W. C. Ho, and D. J. Patnaude, *Mon. Not. R. Astron. Soc.: Lett.* **412**, L108 (2011).
- [5] D. Page, M. Prakash, J. M. Lattimer, and A. W. Steiner, *Phys. Rev. Lett.* **106**, 081101 (2011).
- [6] B. Haskell and A. Melatos, *Int. J. Mod. Phys. D* **24**, 1530008 (2015).
- [7] T. W. B. Kibble, *J. Phys. A* **9**, 1387 (1976).
- [8] W. H. Zurek, *Nature (London)* **317**, 505 (1985).
- [9] P. C. Hendry, N. S. Lawson, R. A. M. Lee, P. V. E. McClintock, and C. D. H. Williams, *Nature (London)* **368**, 315 (1994).
- [10] J. R. Anglin and W. Ketterle, *Nature (London)* **416**, 211 (2002).
- [11] N. P. Proukakis, D. W. Snoke, and P. B. Littlewood, *Universal Themes of Bose-Einstein Condensation* (Cambridge University Press, Cambridge, UK, 2017).
- [12] S. Ritter, A. Öttl, T. Donner, T. Bourdel, M. Köhl, and T. Esslinger, *Phys. Rev. Lett.* **98**, 090402 (2007).
- [13] J. Beugnon and N. Navon, *J. Phys. B: At., Mol. Opt. Phys.* **50**, 022002 (2017).
- [14] M. Gring, M. Kuhnert, T. Langen, T. Kitagawa, B. Rauer, M. Schreitl, I. Mazets, D. A. Smith, E. Demler, and J. Schmiedmayer, *Science* **337**, 1318 (2012).
- [15] C. Eigen, J. A. P. Glidden, R. Lopes, E. A. Cornell, R. P. Smith, and Z. Hadzibabic, *Nature (London)* **563**, 221 (2018).
- [16] J. A. P. Glidden, C. Eigen, L. H. Dogra, T. A. Hilker, R. P. Smith, and Z. Hadzibabic, *Nat. Phys.* **17**, 457 (2021).
- [17] B. Nowak, J. Schole, D. Sexty, and T. Gasenzer, *Phys. Rev. A* **85**, 043627 (2012).
- [18] A. Rañçon and K. Levin, *Phys. Rev. A* **90**, 021602(R) (2014).
- [19] L. E. Sadler, J. M. Higbie, S. R. Leslie, M. Vengalattore, and D. M. Stamper-Kurn, *Nature (London)* **443**, 312 (2006).
- [20] P. C. Hohenberg and B. I. Halperin, *Rev. Mod. Phys.* **49**, 435 (1977).
- [21] K. Damle, S. N. Majumdar, and S. Sachdev, *Phys. Rev. A* **54**, 5037 (1996).
- [22] A. Lamacraft, *Phys. Rev. Lett.* **98**, 160404 (2007).
- [23] A. Polkovnikov, K. Sengupta, A. Silva, and M. Vengalattore, *Rev. Mod. Phys.* **83**, 863 (2011).
- [24] C. Gogolin and J. Eisert, *Rep. Prog. Phys.* **79**, 056001 (2016).
- [25] S. Bhattacharyya, J. F. Rodriguez-Nieva, and E. Demler, *Phys. Rev. Lett.* **125**, 230601 (2020).
- [26] J. Deng, S. Schlichting, R. Venugopalan, and Q. Wang, *Phys. Rev. A* **97**, 053606 (2018).
- [27] J. F. Rodriguez-Nieva, *Phys. Rev. B* **104**, L060302 (2021).
- [28] T. Mitra, A. Mukhopadhyay, and A. Soloviev, *Phys. Rev. D* **103**, 076014 (2021).
- [29] S. Dyachenko, A. C. Newell, A. Pushkarev, and V. E. Zakharov, *Physica D* **57**, 96 (1992).

- [30] C. Connaughton, C. Josserand, A. Picozzi, Y. Pomeau, and S. Rica, *Phys. Rev. Lett.* **95**, 263901 (2005).
- [31] S. Nazarenko and M. Onorato, *Physica D* **219**, 1 (2006).
- [32] V. Shukla, M. Brachet, and R. Pandit, *New J. Phys.* **15**, 113025 (2013).
- [33] S. Nazarenko, M. Onorato, and D. Proment, *Phys. Rev. A* **90**, 013624 (2014).
- [34] M. Prüfer, P. Kunkel, H. Strobelt, S. Lannig, D. Linnemann, C.-M. Schmied, J. Berges, T. Gasenzer, and M. K. Oberthaler, *Nature (London)* **563**, 217 (2018).
- [35] S. Erne, R. Bücker, T. Gasenzer, J. Berges, and J. Schmiedmayer, *Nature (London)* **563**, 225 (2018).
- [36] E. Levich and V. Yakhot, *J. Phys. A* **11**, 2237 (1978).
- [37] D. W. Snoke and J. P. Wolfe, *Phys. Rev. B* **39**, 4030 (1989).
- [38] Y. M. Kagan, B. V. Svistunov, and G. V. Shlyapnikov, *Zh. Eksp. Teor. Fiz.* **101**, 528 (1992) [*Sov. Phys. JETP* **75**, 387 (1992)].
- [39] B. V. Svistunov, *J. Mosc. Phys. Soc.* **1**, 373 (1991).
- [40] D. V. Semikoz and I. I. Tkachev, *Phys. Rev. Lett.* **74**, 3093 (1995).
- [41] D. V. Semikoz and I. I. Tkachev, *Phys. Rev. D* **55**, 489 (1997).
- [42] C. Connaughton and Y. Pomeau, *C. R. Phys.* **5**, 91 (2004).
- [43] N. G. Berloff and B. V. Svistunov, *Phys. Rev. A* **66**, 013603 (2002).
- [44] D. Proment, S. Nazarenko, and M. Onorato, *Phys. Rev. A* **80**, 051603(R) (2009).
- [45] D. Proment, S. Nazarenko, and M. Onorato, *Physica D* **241**, 304 (2012).
- [46] M. J. Davis, S. A. Morgan, and K. Burnett, *Phys. Rev. Lett.* **87**, 160402 (2001).
- [47] P. B. Blakie, A. S. Bradley, M. J. Davis, R. J. Ballagh, and C. W. Gardiner, *Adv. Phys.* **57**, 363 (2008).
- [48] G. Krstulovic and M. Brachet, *Phys. Rev. E* **83**, 066311 (2011).
- [49] N. G. Berloff, M. Brachet, and N. P. Proukakis, *Proc. Natl. Acad. Sci. USA* **111**, 4675 (2014).
- [50] R. H. Kraichnan and D. Montgomery, *Rep. Prog. Phys.* **43**, 547 (1980).
- [51] S. Nazarenko, *Wave Turbulence* (Springer, Berlin, 2011), Vol. 825.
- [52] V. Shukla, A. Gupta, and R. Pandit, *Phys. Rev. B* **92**, 104510 (2015).
- [53] Y. Lvov, S. Nazarenko, and R. West, *Physica D* **184**, 333 (2003), complexity and Nonlinearity in Physical Systems – A Special Issue to Honor Alan Newell.
- [54] R. Lacaze, P. Lallemand, Y. Pomeau, and S. Rica, *Physica D* **152**, 779 (2001).
- [55] B. V. Semisalov, V. N. Grebenev, S. B. Medvedev, and S. V. Nazarenko, *Communications in Nonlinear Science and Numerical Simulation* **102**, 105903 (2021).
- [56] N. Navon, A. L. Gaunt, R. P. Smith, and Z. Hadzibabic, *Nature (London)* **539**, 72 (2016).
- [57] G. V. Kolmakov, P. V. E. McClintock, and S. V. Nazarenko, *Proc. Natl. Acad. Sci. USA* **111**, 4727 (2014).
- [58] Y. B. Zel'dovich and Y. P. Raizer, in *Physics of Shock-Waves and High-Temperature Hydrodynamic Phenomena*, edited by W. D. Hayes and R. F. Probstein (Academic Press, New York, 1967), Vol. 2.
- [59] N. Bogolubov, *J. Phys.* **11**, 23 (1947).
- [60] P. Debue, V. Shukla, D. Kuzay, D. Faranda, E.-W. Saw, F. Daviaud, and B. Dubrulle, *Phys. Rev. E* **97**, 053101 (2018).
- [61] <http://www.fftw.org>.
- [62] Although numerically solving conservative GPE, in the absence of forcing and dissipation, we keep the time step small enough in order to keep nonconservation error to less than 0.1%. In the simulations presented here $\Delta t \sim 10^{-4}$, which gives $t^*/\Delta t \sim 500$ in a typical simulation.
- [63] Note that the presence of a nonzero seed facilitates the triggering of the initial cascade, thereby shortening the nonuniversal transient behavior.
- [64] N. N. Bogolubov, Jr., *Quantum Statistical Mechanics: Selected Works of NN Bogolubov* (World Scientific, Singapore, 2014).
- [65] Even though the ST spectra are averaged on the (k_x, k_z) plane, the δ_ω curve is noisy at high k 's. The noisy signal is a manifestation of the WT discreteness, namely, the fact that the strength of nonlinear interaction, and, therefore, the frequency broadening, is greatly varying depending on how close the discrete k modes are to exact four-wave resonances.
- [66] S. Nazarenko, *J. Stat. Mech.: Theory Exp.* (2006) L02002.
- [67] V. Borue and S. A. Orszag, *Europhys. Lett.* **29**, 687 (1995).
- [68] N. E. L. Haugen and A. Brandenburg, *Phys. Rev. E* **70**, 026405 (2004).
- [69] U. Frisch, S. Kurien, R. Pandit, W. Pauls, S. S. Ray, A. Wirth, and J.-Z. Zhu, *Phys. Rev. Lett.* **101**, 144501 (2008).